Molecular Imaging
Volume 17: 1-11

DOI: 10.1177/1536012118789314
journals.sagepub.com/home/mix
SAGE

Capturing Bone Signal in MRI of Pelvis, as a Large FOV Region, Using TWIST Sequence and Generating a 5-Class Attenuation Map for Prostate PET/MRI Imaging

Mehdi Shirin Shandiz, PhD[1], Hamid Saligheh Rad, PhD[2,3], Pardis Ghafarian, PhD[4,5], Khadijeh Yaghoubi, MSc[1], and Mohammad Reza Ay, PhD[2,3]

Abstract

Purpose: Prostate imaging is a major application of hybrid positron emission tomography/magnetic resonance imaging (PET/MRI). Currently, MRI-based attenuation correction (MRAC) for whole-body PET/MRI in which the bony structures are ignored is the main obstacle to successful implementation of the hybrid modality in the clinical work flow. Ultrashort echo time sequence captures bone signal but needs specific hardware–software and is challenging in large field of view (FOV) regions, such as pelvis. The main aims of the work are (1) to capture a part of the bone signal in pelvis using short echo time (STE) imaging based on time-resolved angiography with interleaved stochastic trajectories (TWIST) sequence and (2) to consider the bone in pelvis attenuation map (μ-map) to MRAC for PET/MRI systems.

Procedures: Time-resolved angiography with interleaved stochastic trajectories, which is routinely used for MR angiography with high temporal and spatial resolution, was employed for fast/STE MR imaging. Data acquisition was performed in a TE of 0.88 milliseconds (STE) and 4.86 milliseconds (long echo time [LTE]) in pelvis region. Region of interest (ROI)-based analysis was used for comparing the signal-to-noise ratio (SNR) of cortical bone in STE and LTE images. A hybrid segmentation protocol, which is comprised of image subtraction, a Fuzzy-based segmentation, and a dedicated morphologic operation, was used for generating a 5-class μ-map consisting of cortical bone, air cavity, fat, soft tissue, and background ($\mu\text{-map}_{\text{MR-5c}}$). A MR-based 4-class μ-map ($\mu\text{-map}_{\text{MR-4c}}$) that considered soft tissue rather than bone was generated. As such, a bilinear ($\mu\text{-map}_{\text{CT-ref}}$), 5 ($\mu\text{-map}_{\text{CT-5c}}$), and 4 class μ-map ($\mu\text{-map}_{\text{CT-4c}}$) based on computed tomography (CT) images were generated. Finally, simulated PET data were corrected using $\mu\text{-map}_{\text{MR-5c}}$ (PET-MRAC5c), $\mu\text{-map}_{\text{MR-4c}}$ (PET-MRAC4c), $\mu\text{-map}_{\text{CT-5c}}$ (PET-CTAC5c), and $\mu\text{-map}_{\text{CT-ref}}$ (PET-CTAC).

Results: The ratio of SNR_{bone} to $\text{SNR}_{\text{air cavity}}$ in LTE images was 0.8, this factor was increased to 4.4 in STE images. The Dice, Sensitivity, and Accuracy metrics for bone segmentation in proposed method were 72.4% $\pm$ 5.5%, 69.6% $\pm$ 7.5%, and 96.5% $\pm$ 3.5%, respectively, where the segmented CT served as reference. The mean relative error in bone regions in the simulated PET images were $-13.98\% \pm 15\%$, $-35.59\% \pm 15.41\%$, and $1.81\% \pm 12.2\%$, respectively, in PET-MRAC5c, PET-MRAC4c, and PET-CTAC5c where PET-CTAC served as the reference. Despite poor correlation in the joint histogram of $\mu\text{-map}_{\text{MR-4c}}$ versus $\mu\text{-map}_{\text{CT-5c}}$ ($R^2 > 0.78$) and PET-MRAC4c versus PET-CTAC5c ($R^2 = 0.83$), high correlations were observed in $\mu\text{-map}_{\text{MR-5c}}$ versus $\mu\text{-map}_{\text{CT-5c}}$ ($R^2 > 0.94$) and PET-MRAC5c versus PET-CTAC5c ($R^2 > 0.96$).

[1] Department of Medical Physics, Zahedan University of Medical Sciences, Zahedan, Iran
[2] Department of Medical Physics and Biomedical Engineering, Tehran University of Medical Sciences, Tehran, Iran
[3] Research Center for Molecular and Cellular Imaging, Tehran University of Medical Sciences, Tehran, Iran
[4] Chronic Respiratory Diseases Research Center, National Research Institute of Tuberculosis and Lung Diseases (NRITLD), Shahid Beheshti University of Medical Sciences, Tehran, Iran
[5] PET/CT and Cyclotron Center, Masih Daneshvari Hospital, Shahid Beheshti University of Medical Sciences, Tehran, Iran

Submitted: 01/03/2018. Revised: 01/05/2018. Accepted: 31/05/2018.

Corresponding Author:
Mohammad Reza Ay, PhD, Department of Medical Physics and Biomedical Engineering, Tehran University of Medical Sciences, Tehran, Iran.
Email: mohammadreza_ay@tums.ac.ir

Conclusions: According to the $SNR_{STE,\ pelvic\ bone}$, the cortical bone can be separate from air cavity in STE imaging based on TWIST sequence. The proposed method generated an MRI-based μ-map containing bone and air cavity that led to more accurate tracer uptake estimation than MRAC4c. Uptake estimation in hybrid PET/MRI can be improved by employing the proposed method.

Keywords
PET/MRI, MRI-based attenuation correction, μ map, TWIST sequence, prostate imaging

Introduction

There has been much research interest in clinical applications of positron emission tomography/magnetic resonance imaging (PET/MRI).[1] This has increased since the introduction of integrated PET/MRI technology that provides simultaneous PET and MRI imaging.[1] The use of this technology in hybrid PET/MRI imaging can overcome the problem of mismatching in sequential hybrid imaging methods such as PET/computed tomography (CT).[1] Owing to the intrinsic properties of MRI, the advantages of PET/MRI over PET/CT include higher contrast for soft tissue, higher sensitivity in identification of bone metastases, extra information about lesions through the potential for MRI anatomical and functional imaging,[2] and most importantly, enabling a further reduction in the absorbed dose provided by medical radiation exposure.[1,3] Such merits are important, particularly in challenging anatomic regions such as the pelvis and prostate in terms of image appearance and interpretation.[2] Despite these advantages, PET/MRI systems suffer from inaccurate attenuation correction (AC). From the clinical standpoint, comparable accurate standard uptake value (SUV) estimation and acquisition time relative to PET/CT are necessary for successful implementation of PET/MRI in the clinical workflow.[4]

In contrast with CT imaging, MR data does not correlate with electron density, which is an indication of tissue attenuation. As a result, it is impossible to obtain a μ-map directly from an MR image ($\mu\text{-map}_{MR}$) like from CT ($\mu\text{-map}_{CT}$). MRI-based attenuation correction (MRAC) techniques include segmentation-based (SEG-AC),[5,6] atlas/template-based (AT-AC),[7,8] model-based (Model-AC),[9] and emission data-based AC.[10] As such, there are techniques based on dedicated imaging such as the ultrashort (UTE-AC), zero (ZTE-AC), and short echo time (STE-AC).[7,9,11-14] In SEG-AC approaches currently employed in PET/MRI systems, MR images are classified quickly and directly into several classes in which bone structure is substituted by soft tissue in the relevant μ-map.[5,6] Initial studies had shown that ignoring bone has no noticeable impact on PET quantification[5,6]; however, recent studies have indicated that assigning soft tissue rather than bone to μ-maps has a noticeable impact on SUV, particularly in osseous lesions located in thick cortical bones such as the pelvis.[15-18]

Although commercially available prototypes of Model-AC,[9] and AT-AC methods[7] are reliable and robust in rigid regions with normal anatomy such as the head, their behavior in nonrigid regions such as the pelvis or organs with anatomical variations are unclear.[13] Moreover, AT-AC methods tend to err in nonrigid regions such as the thorax and pelvis.[13,19] Although atlas/pattern recognition-based approaches introduced by Hofmann et al[15] and Arabi and Zaidi[20] perform better than pure AT-based approaches, they cause problems owing to the registration step.[21] Registration is time consuming and error-prone, especially in a nonrigid region with a large field of view (FOV) such as the pelvis.[21]

Ultrashort echo time and ZTE MRI sequences, which can differentiate air from tissue with short transverse relaxation times such as cortical bone, have been introduced for direct and more accurate μ-map generation. Currently, ZTE-AC and UTE-AC are commercial available prototypes in PET/MRI systems.[7,22] Although the results of their use on head are promising particularly in newer versions,[7,12,23] their use in a larger FOV is often associated with increasing segmentation error, artifacts, and long acquisition time.[4,13,23] The artifacts are generated by capturing the signal of materials near the radio frequently (RF) coil, such as the RF coating, which blurs images and causes aliasing.[4]

Previously, we observed that a part of the cranial bone signal can be captured using fast low-angle shot (FLASH) sequence with short TE acquisition (TE $\sim$ 0.8-1 milliseconds) and long acquisition time of 462 seconds.[11,24] Although the bone signal intensity is much less than that in UTE, it has a much higher magnitude than noise and is sufficient for cranial bone separation.[11,25] However, in large FOV such as pelvis, there are technical limitations for applying FLASH sequence in TE of submillisecond.[26] Thus, the pelvis bone signal cannot be captured.[26] Time-resolved angiography with interleaved stochastic trajectories (TWIST) sequence,[27] which is routinely used for MR angiography with high temporal and spatial resolution, can be used for fast imaging and applying TEs of submillisecond. The current study used this sequence along with a direct/rapid segmentation strategy to consider cortical bone in the $\mu\text{-map}_{MR}$ of prostate region. The used hybrid segmentation (HSEG) protocol classifies MR images into 5 classes (cortical bone, air cavity, background air, fat, and soft tissue) by subtracting STE and long echo time (LTE) images, object analysis, and applying a dedicated closing-dilating operation.

Materials and Methods

Image Acquisition

Magnetic resonance imaging of the pelvic region was performed using a 1.5T MRI system (upgraded Magnetom

Avanto; Siemens, Germany). For STE imaging, the TWIST sequence, which is routinely used for MR angiography of the carotid arteries with high temporal and spatial resolution,[27] was employed for fast pelvis imaging with a short TE of 0.88 milliseconds. In contrast with FLASH sequences, TWIST can be used in TEs of submillisecond in large FOV regions such as pelvic. As such, data accusation by this sequence is fast.

The sequence was applied to the pelvic organs of 5 volunteers using the following parameters:

Echo time/Repetition time = 0.88/20 milliseconds, flip angle of 15°, bandwidth of 680 Hz/pixel, isotropic voxel size of $1.1 \times 1.1 \times 1.1$ mm^3 with a slab FOV of 20 cm (182 slices), and acquisition time of 168 seconds. Long echo time imaging was performed using volumetric interpolated breath-hold examination with the same parameters as TWIST except for TE (4.86 milliseconds). Ultra-low-dose CT imaging was applied using a 16-slice CT scanner (Siemens, Germany) to generate a μ-map$_{CT}$. The parameters were 120 kVp, 20 mAs, and a voxel size of $1 \times 1 \times 1$ mm^3. This imaging was approved by the Ethical Committee of Tehran University of Medical Sciences (license #1432), and all volunteers signed informed consent forms.

In both CT and MR scans, the participants were supine with arms folded and were positioned by the same technologist to ensure the most similar positioning. The slab FOV was set to the scout view from the iliac crest to 5 cm inferior to the femur neck. To decrease registration error, the CT scan was performed within 10 minutes of the MRI. A Perspex base plate was located on the CT couch to increase similarity of body position in MRI and CT scan.[26] This base plate is used for registration in radiotherapy.

Magnetic Resonance Image Processing

All steps except image registration and reconstruction were implemented in MATLAB (MathWorks). Figure 1A shows the steps employed to generate a 5-class attenuation map (μ-map$_{MR5c}$) for use in MRAC.

Signal-to-noise ratio measurement. The signal-to-noise ratio (SNR) was computed in several regions of interest (ROIs) on bone structures as defined by an expert radiologist. To compute the SNR, the mean intensity of the ROI was divided by the mean intensity (noise) in a similar ROI chosen in the near background area. The same calculation was made in ROIs defined in internal air cavities in both STE and LTE images for reasonable comparison.

Magnetic resonance imaging segmentation. The dedicated HSEG method used to generate the μ-map$_{MR5c}$ is described below. This method was applied on the axial MR images.

Step 1: Fuzzy logic-based image clustering

The STE images were automatically segmented into 3 classes (bone-air, soft tissue, fat; Figure 1A) using the spatial fuzzy c-means (SFCM) approach.[28] In contrast to the fuzzy c-means approach, SFCM fully incorporates local spatial information in the image to reduce misclustering and spurious blobs, especially in noisy images.[26]

Step 2: Separating cortical bone and internal air cavity based on intensity

Because bone and internal air structures have similar intensities in an LTE image with a TE of 4.86 milliseconds, they were classified in the same cluster by means of SFCM as shown in Figure 1A. Unlike an LTE image, STE image has a part of the low and short-lived bone signal owing to the short TE of 0.88 milliseconds. The main steps for separating cortical bone and internal air structures based on intensity are:

a. The bone-air regions in STE data were extracted by the guidance of corresponding bone–air binary mask of LTE data that were segmented using SFCM. Then, the bone–air regions in STE were subtracted from those in LTE (Figure 1A). Ideally, the bone and air pixels will have positive and 0 values, respectively, in the subtracted images.
b. Because a few bone pixels may have 0 or negative values in the subtracted images (Figures 1 and 3, yellow arrows) owing to the partial volume effect (PVE) or registration error, object-based (not pixel-based) classification was performed to avoid misclassification. The objects in each slice in bone–air binary mask were automatically traced and labeled (Figure 1A), and then bone–air regions in the subtracted images were separated based on the median intensity of the object pixels.
c. A dedicated closing and internal dilating morphologic operation was applied to the bone binary mask (Figure 1B) to recover missing edges and to dilate bony structures. To highlight missing bony edges, the binary bone mask was thinned to a pixel. In this situation, the missed edges have only 1 neighbor and so are highlighted. Then, edge (end point) connection was performed between nearest neighbors. As shown in Figure 1B, the resulted bony mask was dilated (Figure 1A-a) and filled (Figure 1B-b). Intersection (a$\cap$b) of the outcomes of these 2 operations makes an internal dilation. The internal dilation is necessary to improve segmentation results because cortical bone region depicted thinner in MRI relative to CT images.[11]

Step 3: Background segmentation

The Chan-Vese active contour was employed to extract the background (external air) of the pelvic MR images. A circular initial contour defined in the center of the image evolved to capture the boundary of the body and separate it from the background.

Step 4: μ-map$_{MR}$ generation

The masks of the cortical bone, internal air cavity, background, soft tissue, and fat were added to a 0 matrix (Figure 1A), and the voxel size was downsampled to

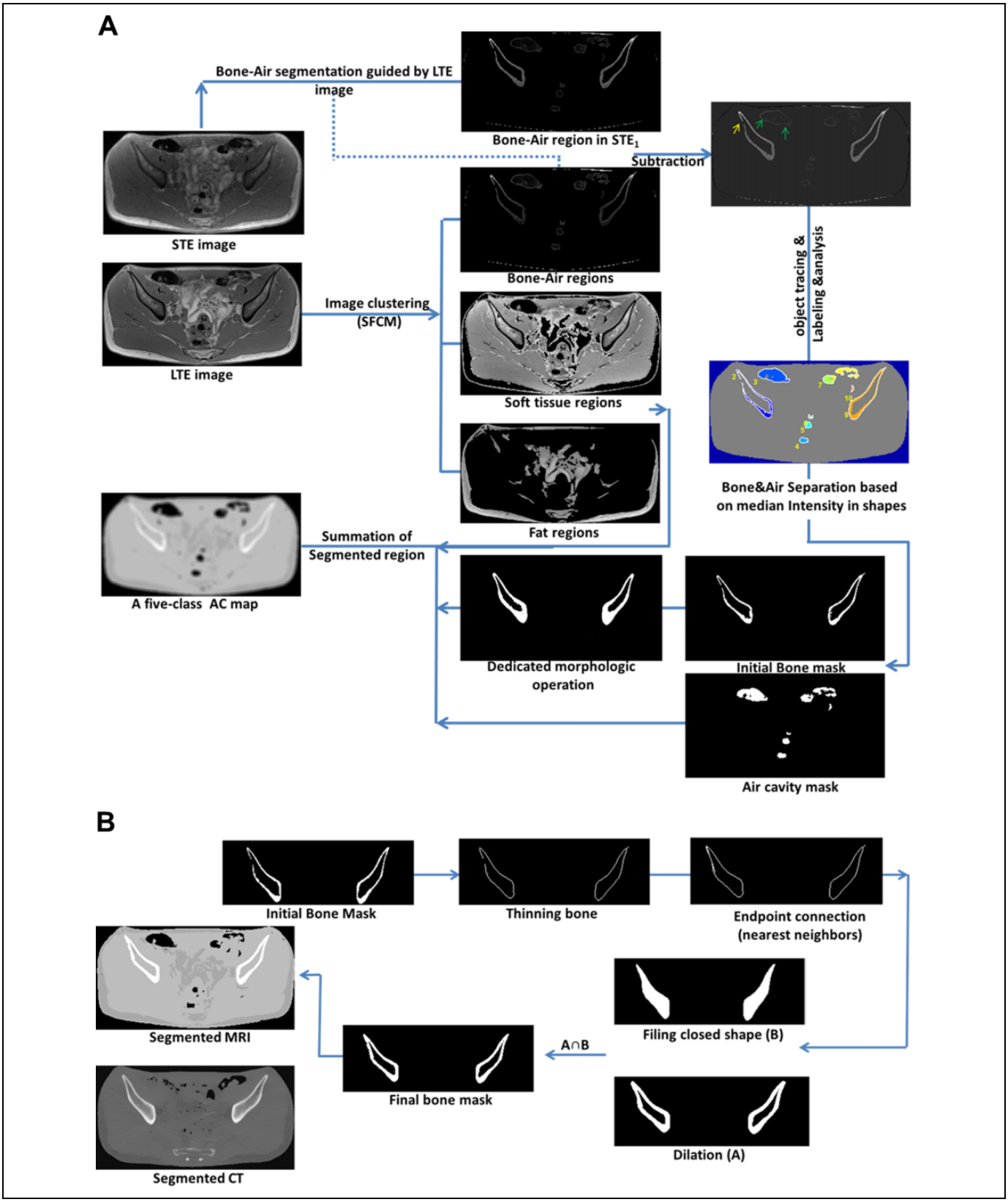

Figure 1. (A) the workflow of the proposed hybrid segmentation (HSEG) method for segmenting axial MR images and generating a 5-class μ-map. (B) A dedicated closing and internal dilating morphologic operation for decreasing the segmentation error. Yellow (bone) and green (air) arrows show some pixels in the bone–air subtraction slices that have wrong value owing to PVE. PVE indicates partial volume effect.

$4 \times 4 \times 4$ mm^3. Attenuation coefficients of the tissues at 511 keV were assigned to each mask.[5,18] The assigned values were 0.13 cm^{-1}, 0.0003 cm^{-1}, 0.0003 cm^{-1}, 0.096 cm^{-1}, and 0.086 cm^{-1} for cortical bone, internal air cavity, background, soft tissue and fat, respectively.[5,18] The generated map was smoothed using a 3D Gaussian kernel with an full width at half maximum (FWHM) of 5 mm to generate the μ-map$_{MR5c}$. This map was used for the MRI-based 5-class AC (MRAC5c) on simulated PET data (PET-MRAC5c). For an MRI-based 4-class AC (MRAC4c) similar to Dixon-based 4-class direct segmentation approach proposed by the Martinez-Möller et al,[5] the values assigned to cortical bone and soft tissue were changed to 0.10 cm^{-1} to yield a 4-class attenuation map (μ-map$_{MR4c}$).

Computed Tomography Image Processing

Segmented CT data were used as a reference to assess the performance of HSEG. The 3-D CT images were registered on 3-D MR images after preprocessing for better registration.[26] The main preregistration stages were couch and background removal from CT data and CT image denoising. The first 2 stages were done by means of the Chan-Vese active contour. For CT denoising, the nonlocal mean filter was used.

Image registration. The 3D registration of CT to STE images was performed using the Elastix package as based on the insight segmentation and registration toolkit.[29] As described previously,[18,26] because the pelvic region is nonrigid, a 2-step registration comprising affine and b-spline transformation were applied to CT images to achieve close to perfect alignment between the CT and the MR data.[18,26] The registration results were assessed using Dice and Jaccard metrics.

Computed tomography segmentation and μ-map$_{CT}$ generation. The deformed CT images were downsampled to a voxel size of $4 \times 4 \times 4$ mm^3, and the Hounsfield unit was transformed into an attenuation coefficient in 511 keV using bilinear transformation to generate the reference CT-derived μ-map (μ-map$_{CTref}$) for use in CTAC. To evaluate the performance of HSEG in generating μ-map$_{MR5c}$, a CT-derived 5-class μ-map (μ-map$_{CT5c}$) with predefined attenuation coefficients was generated. The thresholding values in the segmented CT were cortical bone ($I \geq 140$ HU), soft tissue ($-20\text{HU} \leq I < 140$ HU), fat tissue (-470 HU $< I < -20$ HU), internal air ($I \leq -470$ HU), and background ($I < -470$ HU).[5,18] Note that the same attenuation coefficients used in μ-map$_{MR5c}$ were assigned to μ-map$_{CT5c}$. To generate a typical μ-map, the maps were smoothed using a 3-D Gaussian kernel with an FWHM of 5 mm.

Segmentation Assessment

To evaluate the accuracy and robustness of the proposed segmentation method, the Sensitivity, Accuracy, Dice, and Jaccard metrics were calculated by pixel-by-pixel comparison between the segmented MR and CT as:

$$\text{Sensitivity} = \frac{\text{TP}}{(\text{TP} + \text{FN})} \times 100 \quad (1)$$

$$\text{Accurracy} = \frac{(\text{TP} + \text{TN})}{(\text{TP} + \text{FN} + \text{FP} + \text{TN})} \times 100 \quad (2)$$

$$\text{Dice} = \frac{2(\text{TP})}{(2\text{TP} + \text{FN} + \text{FP})} \times 100 \quad (3)$$

$$\text{Jaccard} = \frac{\text{TP}}{(\text{TP} + \text{FN} + \text{FP})} \times 100 \quad (4)$$

where CT-based segmentation results were considered as ground truth (reference) in order to calculate the parameters of false positive (FP), false negative (FN), true positive (TP), and true negative (TN). These metrics were calculated for cortical bone, soft tissue, fat, and air cavities. It should be note that although 5 volunteers were considered in this study, but in fact 270 slices (54 slices in each participant) which have varied complexity were used for the assessment of the HSEG. Moreover, the performance of μ-map$_{MR}$ versus μ-map$_{CT}$ was depicted in a joint histogram and calculated using the correlation coefficient. All slices except those having noticeable registration error were employed for segmentation assessment.

Quantitative Evaluation

Positron emission tomography data simulation. To compare the effects of μ-map$_{MR}$ and μ-map$_{CT}$ in AC on PET data, anthropomorphic numerical phantoms of the pelvis were generated from CT data (Figure 2) by simulating the average 18 F-fluorodeoxy-glucose (FDG) uptake of a normal healthy patient.[30] This procedure imitates the generation of emission phantoms from CT data as described by Catana et al.[22] The generated emission phantoms were smoothed using a 3-D Gaussian kernel with an FWHM of 5 mm.

As shown in Figure 2, the simulated PET data was converted to projection data (sinogram) and attenuated with μ-map$_{CTref}$ as the reference CT-derived μ-map and then mixed with Poisson noise to generate PET raw data.[18] The work simulated the geometry of the Biograph 16 Hi-REZ scanner (Siemens, Germany) for generating PET raw data and photon attenuation. Note that the steps of forward projection, photon attenuation, and AC were performed using an software for Tomographic Image Reconstruction (STIR) package.[31]

Attenuation correction. The PET raw data (sinogram) were corrected (for attenuation) using μ-map$_{MR5c}$ (PET-MRAC5c), μ-map$_{MR4c}$ (PET-MRAC4c), μ-map$_{CT5c}$ (PET-CTAC5c), and μ-map$_{CTref}$ (PET-CTAC). They were then reconstructed using ordered subsets-expectation maximization (OSEM) algorithm with parameters (8 subsets, 4 iterations, and a postprocessing Gaussian kernel with a FWHM of 5 mm) adopted in clinical protocols.[20]

To compare the PET-MRAC5c with other corrected PET data, the metrics of relative error (RE), joint histogram, and

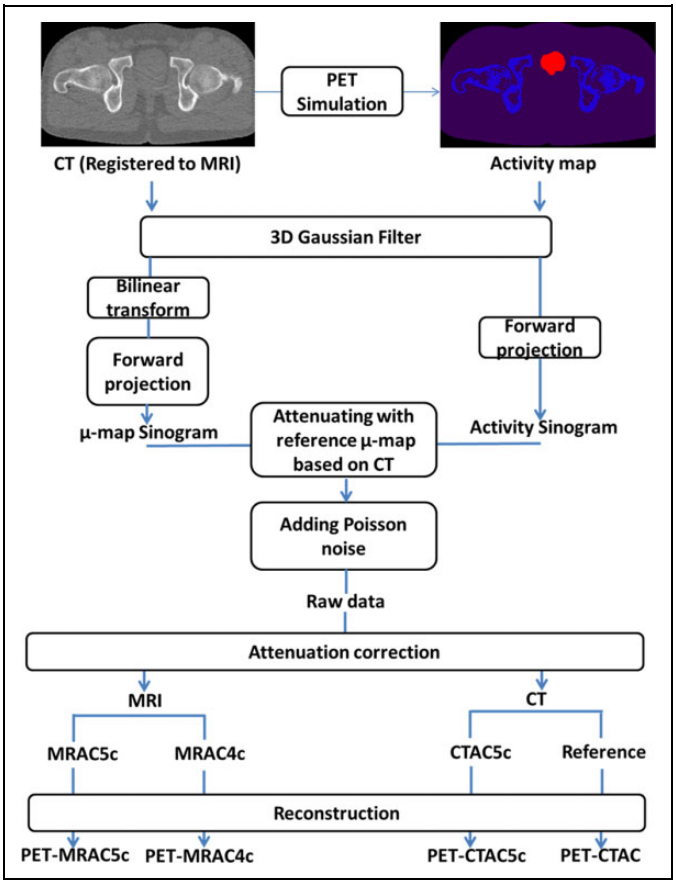

Figure 2. The workflow of simulation PET, PET raw data generation, and attenuation correction with different μ-map. PET indicates Positron emission tomography.

box-whisker plot were employed. The RE map was computed through voxel-by-voxel subtraction of the resulting PET data (PET_r) from the PET-CTAC data as a ground truth (PET_{ref}), dividing PET_{ref} data as follows:

$$RE\ (\%) = \frac{PET_r - PET_{ref}}{PET_{ref}} \times 100 \qquad (5)$$

Region of interest-based analysis was done on the RE maps, and the results were depicted in the box–whisker plot. Note that the 3D ROIs were defined randomly for different sizes (radius of 10-40 mm), locations, and slices. The number of ROIs was based on statistical criteria.

Results

Table 1 presents the SNRs of cortical bone and internal air cavity in pelvic regions for STE and LTE images. While the ratio of SNR_{bone} to $SNR_{air\ cavity}$ in LTE was 0.8, this factor was increased to 4.4 in STE. Figure 3 shows 2 exemplary STE and LTE images with different complexities and their subtraction in bone–air regions. Despite errors (yellow arrows), most bone pixels have positive values (>40), while the air cavities have 0 values. Figure 3D depicts the outcome of separation of the bone–air regions using object analysis (not pixel analysis).

Table 1. The SNR of Bone and Air Cavity in STE and LTE Images Provided by TWIST Sequence.[a]

Imaging Protocol	Region	SNR	$SNR_{Bone}/SNR_{Air\ cavity}$
STE	Bone	27.7 ± 5.5	4.4
	Air cavity	6.3 ± 2.1	
LTE	Bone	6.8 ± 2.9	0.8
	Air cavity	8.5 ± 4.3	

Abbreviations: LTE, long echo time; SNR, signal-to-noise ratio; STE, short echo time; TWIST, time-resolved angiography with interleaved stochastic trajectories.
[a]The data show considerable SNR_{bone} in STE in comparison to LTE imaging.

While separating pixels based on pixel intensity led to misclassification (yellow and green arrows), separating based on median intensity of objects decreased this misclassification. Figure 3E shows the results of the dedicated morphologic operation for connecting missed boundaries (red arrows) and internal dilation (blue arrows) in bone regions. In comparison with CT images, Figure 3F reveals the promising potential of HSEG in bone regions for pelvic MR images.

The performance assessment of HSEG on a pelvic MRI using the Sensitivity, Dice, Accuracy, and Jaccard metrics is summarized in Table 2. Using $\mu\text{-map}_{MR5c}$ provided by HSEG, the Dice, Jaccard, Accuracy, and Sensitivity metrics were 72.4% ± 5.5%, 58.4% ± 7.9%, 96.5% ± 3.5%, and 69.6% ± 7.5%, respectively, in cortical bone structures and 66.6% ± 7.9%, 56.3% ± 7.2%, 89.9% ± 8.1%, and 59.7% ± 7.6%, respectively, in air cavity regions. It should be noted that the segmented CT data which served as a reference in segmentation and quantitative assessments were acceptably matched to LTE images with an average Dice of 93.6% ± 5% and Jaccard of 92.5% ± 2%.

The outcomes of PET data corrected with μ-maps are presented in Table 3 and Figure 4 using PET-CTAC as a reference and ground truth. Region of interest-based analysis shows high negative bias (mean RE) in bone regions in PET-MRAC4c (−35.59 ± 15.41%), while the bias was −13.98% ± 15% in PET-MRAC5c (Table 3 and Figure 4). The negative bias was lower for the ilium (−9.85% ± 9.42%) and iliac (−7.32% ± 11.60%) bones. As shown in Table 3 and in the RE maps in Figure 4, the positive bias in soft tissue in the PET-MRAC5c (3.99% ± 5.76%) was lower than that in PET-MRAC4c (7.52% ± 8.21%). Likewise, overestimation of the fat region in PET-MRAC5c (7.25% ± 11.47%) was lower than that in PET-MRAC4c (8.45% ± 12.97%).

Discussion

Currently, Dixon-based 4-class direct segmentation approach[5,7] is a conventional method to AC in PET/MRI systems for clinical use. This method is patient based as well as fast and robust[19,21]; however, the method made inaccurate AC[16,18] because it ignored cortical bones and ignored[6] or underestimated the volume of internal air cavities in the

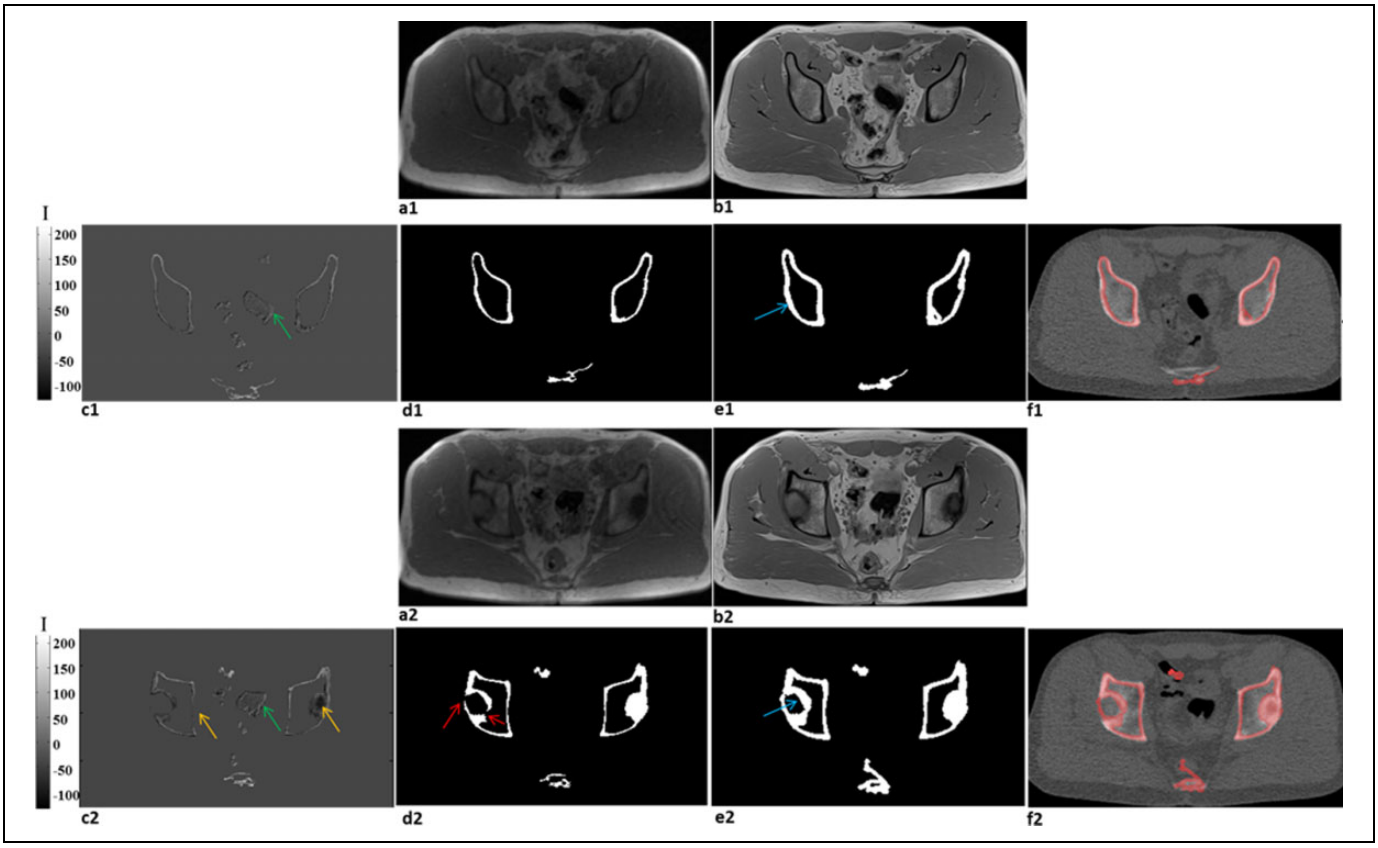

Figure 3. Representative slices of STE data acquisition and bone extraction. (A) STE images. (B) LTE images. (C) Bone extraction based on subtracting 2 STE and LTE images. (D) The bone masks. (E) Applying dedicated closing and internal dilating morphologic operation on bone mask. (F) Overlaying the bone mask on CT images. Yellow (bone) and green (air) arrows show some pixels in the bone-air subtraction slices that have wrong value owing to PVE. Red arrows show missed edge. Blue arrows show internal dilation on bone mask. CT indicates computed tomography; LTE, long echo time; PVE, partial volume effect; STE, short echo time.

Table 2. Performance Assessment of the Hybrid Segmentation Method by Voxel-Wise Comparison.[a]

	Sensitivity	Accuracy	Dice	Jaccard
	Mean (SD), %			
Cortical bone	69.6 (7.5)	96.5 (3.5)	72.4 (5.5)	58.4 (7.9)
Internal air	59.7 (7.6)	89.9 (8.1)	66.6 (7.9)	56.3 (7.2)
Soft tissue	97 (5.9)	97.8 (3.2)	96.6 (3.3)	95.5 (4.5)
Fat	67.6 (6.6)	95.8 (4.2)	78 (6.9)	67 (8)

Abbreviations: CT, computed tomography; SD, standard deviation.
[a]The segmented CT is considered as reference.

Table 3. Quantitative Comparison of PET-MRAC5c and Other Attenuation Corrected PET Data.[a]

	RE (%), PET-CTAC as ground truth		
Region	PET-MRAC5c	PET-MRAC4c	PET-CTAC5c
Bone	−13.98 ± 15	−35.59 ± 15.41	1.81 ± 12.2
Soft tissue	3.99 ± 5.76	7.52 ± 8.21	−0.4 ± 1.82
Fat	7.25 ± 11.47	8.45 ± 12.97	1.16 ± 2.32
Ilium	−9.85 ± 9.42	−38.75 ± 16.72	−5.21 ± 8.1
Iliac	−7.32 ± 11.60	−40.33 ± 14.16	1.58 ± 11.87
Femoral head	−28.83 ± 15.92	−32.63 ± 17.4	6.2 ± 5.95
Prostate	3.76 ± 2.19	7.35 ± 2.72	−0.06 ± 0.86
Thin bone	−5.85 ± 4.21	−2.24 ± 4.25	9.34 ± 3.19

Abbreviations: PET, positron emission tomography; RE, relative error; ROI, region of interest.
[a]Analysis was done on random ROI defined in different regions.

μ-map.[5] Although the performance of commercially available prototypes such as Model-AC,[9] AT-AC,[7] UTE-AC,[22] and ZTE-AC[7] are promising in head, their behavior in pelvis, as large FOV and nonrigid region are unclear.[13] The present study, as a direct segmentation approach, considered cortical bones and internal air cavities in the pelvic μ-map. To the best of our knowledge, this is the first study that takes into account cortical bones and air cavities in the pelvis μ-map using the aforementioned strategy. In present work, bone segmentation was performed based on the subtraction of 2 images (STE and LTE) together with dedicated and HSEG method.

The SNR_{bone} to $SNR_{air\ cavity}$ ratio in STE relative to LTE imaging (Table 1) and the bone–air subtraction slices (Figure 3C) indicate that STE imaging with a TE of 0.88 milliseconds was successful in capturing a part of the low and short-

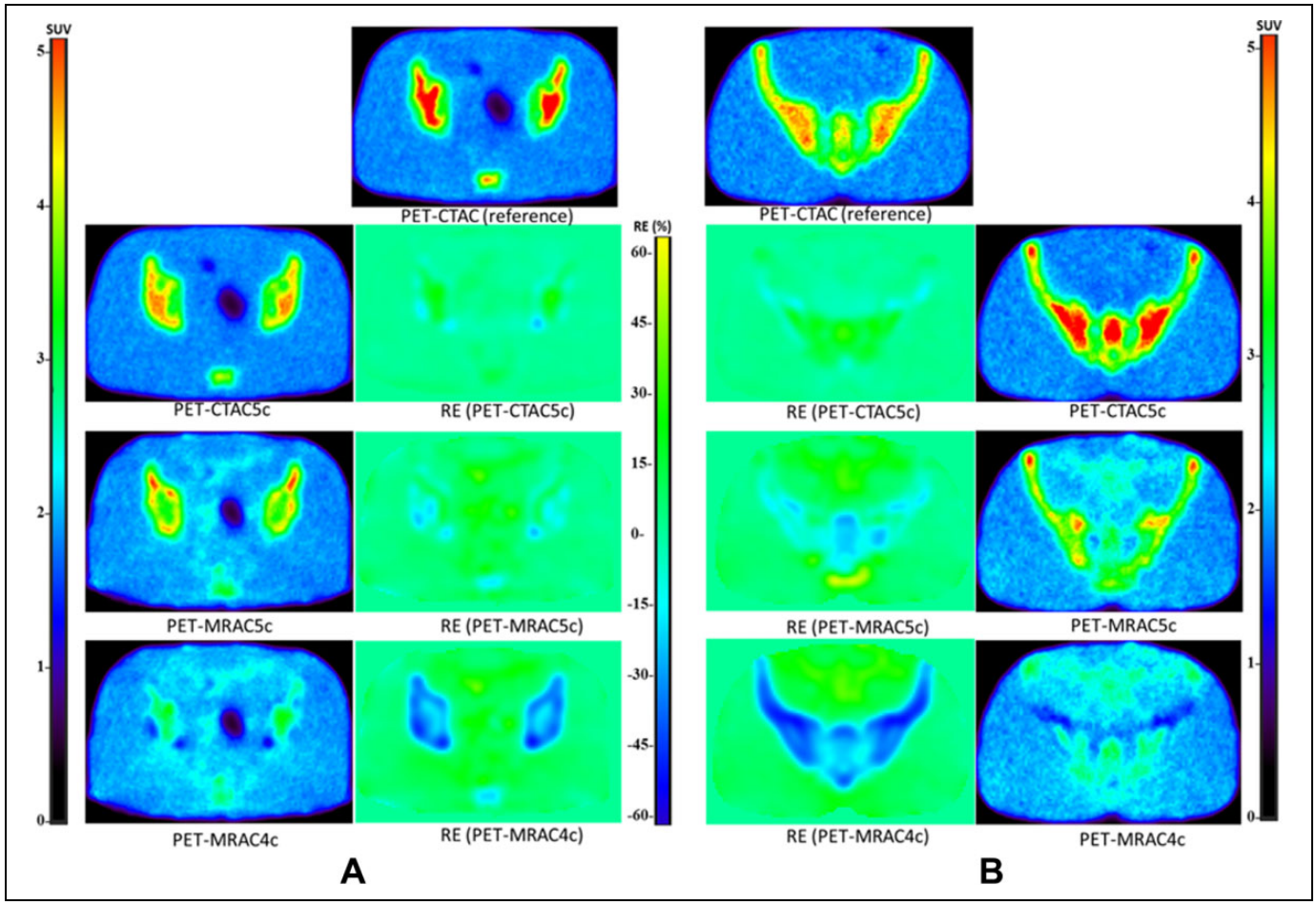

Figure 4. The PET data corrected with different μ-maps and corresponding error maps for 2 sample slices. The reference PET images are PET-CTAC data which are corrected by reference μ-map (μ-map$_{CTref}$). b1 and b4; c1 and c4; and d1 and d4 are PET-CTAC5c, PET-MRAC5c, and PET-MRAC4c, respectively while b2 and b3; c2 and c3; and d2 and d3 are corresponding error maps.

lived MR bone signals in the pelvic region. The receipt of signals of bone using the TWIST sequence in this TE is important because it can be used to differentiate bone regions from air cavities during segmentation. FLASH sequences can be utilized for TEs of submillisecond in a rather small FOV.[11] But, FLASH sequences are not particularly useful in the pelvic region because they are time consuming[11] and have technical limitation for applying short TEs in a large FOV.[26] Khateri et al reported an acquisition time of 462 seconds for FLASH-based STE imaging of the head region.[11] Segmentation based on STE[11] is advised because UTE and ZTE imaging is associated with artifacts[4,13] and is time consuming for a large FOV.[13]

Visual inspection of the bone–air subtraction slices in Figure 3 shows that separation of pixels based on pixel value could cause misclassification of some pixels (yellow and green arrows) owing to PVE.[4] Object analysis and separation of bone–air objects based on average intensity of pixels of objects (Figure 3D) and applying dedicated dilation-closing method (red vs blue arrows) considerably improved segmentation performance. Table 2 and Figure 3D-F show the performance of HSEG to segment cortical bone (Dice of 72.4% ± 5.5%; Sensitivity of 69.6% ± 7.5%), where CT data at Hu ≥ 140 served as the reference. A sensitivity of 40% ± 15% and dice of 58% ± 9% have been reported by Hofmann et al[15] and a

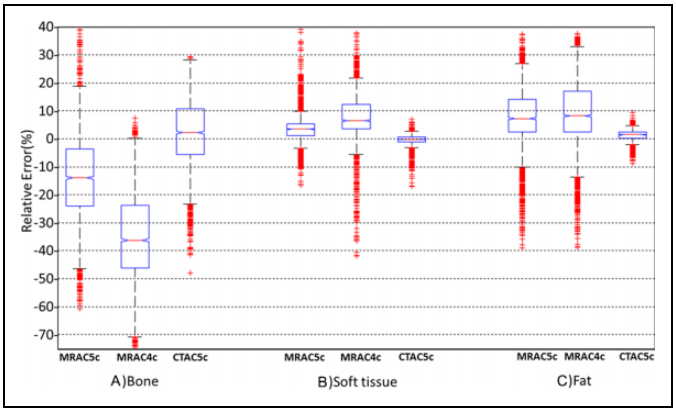

Figure 5. Box-whisker plots illustrating the statistical analysis of the error map for attenuation corrected PET data. The plots are based on randomly ROI selection in bone, soft tissue, and fat. ROI indicates region of interest.

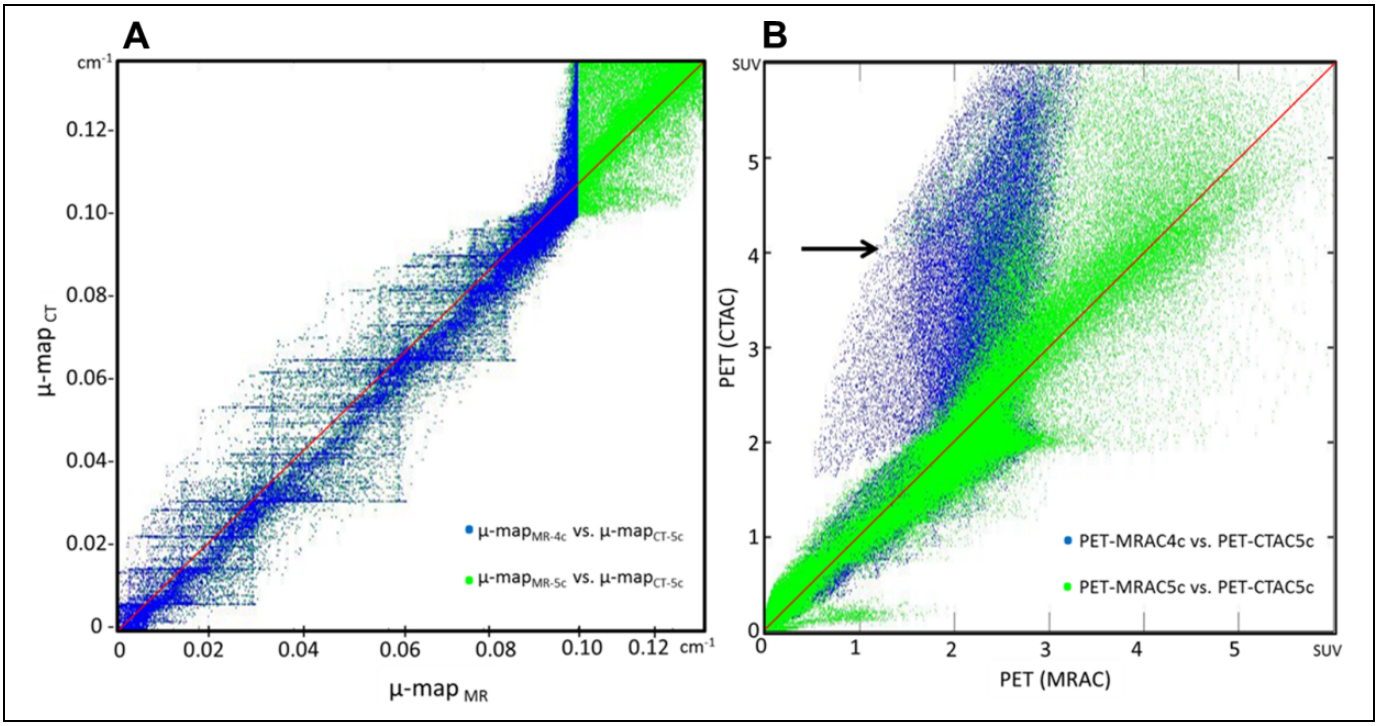

Figure 6. Joint histograms and coloration coefficients of μ-map$_{CT5C}$ with μ-map$_{MR5C}$ and μ-map$_{MR4C}$ (A) as well as PET-CTAC5c versus PET-MRAC5c and PET-MRAC4c. (B) The black arrow show the deviation in the joint histograms of μ-map$_{MR4c}$ vs μ-map$_{CT5c}$ at $\mu = 0.10$ cm^{-1}.

sensitivity of 48% ± 12% and dice of 41% ± 5% by Arabi and Zaidi.[20] Dual UTE-based segmentations, of which the current work is an adaptation, experience problems in a large FOV[5,13]; thus, they are promising only in the head region. The previously reported performances with a dice of 69% (Cabello et al), 75% (Juttukonda et al), and 49% (Delso et al) for UTE-based segmentation methods that the data are similar to the current results.[32-34] As such, dice in the HSEG method is comparable to a hybrid approach proposed by An et al for head region (dice of 79% ± 2%).[23] The method is comprised of level-set segmentation and UTE imaging that even has better performance relative to Siemens Biograph mMR (Software version VB20P) (dice of 72% ± 4%).[23]

Although Dixon-based 4-class segmentation approach proposed by Martinez-Möller et al[5] ignored considerable air cavities, the HSEG method notably extracted them (Dice of 66.6% ± 7.9%; Accuracy of 89.9% ± 8.1%) as illustrated in Table 2 and Figure 3. The results are comparable with the performance of UTE-based segmentation method used in VB20P mMR software in head (60% ± 6%).[23] Because the pelvic region often contains large air cavities, replacing soft tissue with air in the μ-map will affect local activity and even global activity owing to the 3-D reconstruction.[16,18]

The promising performances of SFCM for clustering soft tissue (Dice of 96.6% ± 3.3%) and fat (Dice of 78% ± 6.9%) are presented in Table 2. The SFCM algorithm described previously[26,35] directly clusters the pixels of an image using fuzzy logic. The Dixon technique employed in triple UTE[13] and the Martinez-Möller's approach[5] requires twice data acquisition and is error prone in phase wrapping and noise.[13] Overall, the current results show the special potential of the HSEG relative to the morphologic intensity and AT, UTE-based segmentation methods.[15,20,23,26,35,36]

The results of ROI-based analysis on PET data corrected using different μ-maps (Figure 4) are presented in Tables 3 and in the box-whisker plots in Figure 5 where PET-CTAC considered as ground truth. The data show the bias for all regions in PET-MRAC5c are lower than those in PET-MRAC4c. MRAC4c in soft tissue and prostate regions yielded average REs of 7.52% ± 8.21% and 7.35% ± 2.72%, respectively, using MRAC5c yielded 3.99% ± 5.76% and 3.76% ± 2.19%, respectively. It appears that assigning a higher μ (0.10 cm^{-1}) to soft tissue in MRAC4c relative to MRAC5c results in greater positive bias.[9] These outcomes are in agreement with literature.[9,9,20,36,37] Leynes et al reported the root mean square error (RMSE) of 7.79% using MRAC4c and 3.94% using a Hybrid ZTE/Dixon-based AC in pelvis region.[36]

As shown in the box–whisker plots (Figure 5) and Table 3, negative bias in the bone regions in PET-MRAC4c is high (−35.59% ± 15.41%) while in PET-MRAC5c (−13.98% ± 15%) significantly ($P < .0001$) decreased. This improvement was even higher in thick bones such as the iliac (−7.32% ± 11.60%) and ilium (−9.85% ± 9.42%). Fortunately, this bias was not significantly different between PET-MRAC5c and PET-CTAC5c ($P > .05$), which indicates that μ-map$_{MR5c}$ derived by HSEG is promising for bone regions. The high negative bias in the bony regions of PET-MRAC4c is

consistent with results from Paulus et al (−25%), Hofmann et al (−30%), Marshall et al (−35%), and Akbarzadeh et al (−30%).[9,15,18,38] Although thin bony structures such as the coccyx in the pelvis were inherently missed during segmentation owing to PVE, the results (Tables 3, Figures 4 and 5) show that this miss-segmentation is not effective on the clinical interpretation because the bias was less than 5%.[17] This observation is in accordance with that reported by Samarin et al.[17] However, similar to work of Paulus et al,[9] negative bias in femoral head for PET-MRAC5c is still noticeable.

Unlike the poor correlation in $\mu\text{-map}_{MR4c}$ versus $\mu\text{-map}_{CT5c}$ ($R^2 = 0.78$) and PET-MRAC4c versus PET-CTAC5c ($R^2 = 0.83$), acceptable correlation was observed in $\mu\text{-map}_{MR5c}$ versus $\mu\text{-map}_{CT5c}$ ($R^2 > 0.94$) and PET-MRAC5c versus PET-CTAC5c ($R^2 > 0.96$), as clearly depicted in the joint histograms in Figure 6. The joint histograms of HSEG method are comparable with those in the Hybrid ZTE/Dixon segmentation method introduced by Leynes et al in pelvis region.[36] It appears that the deviation in the joint histograms of $\mu\text{-map}_{MR4c}$ versus $\mu\text{-map}_{CT5c}$ at $\mu = 0.10\ cm^{-1}$ resulted in considerable deviation in the corresponding PET data (Figure 6B; black arrow). The deviations in the joint histograms of PET-MRAC5c versus PET-CTAC5c such as the SUV of 3 have arisen from misclassification in HSEG.

As mentioned, the SEG-AC approaches led to inaccurate distribution of PET tracer.[6,19] Both, UTE-AC and ZTE-AC, result in artifacts and miss-segmentation in particular in organs with a large FOV.[13] On the other hand, AT-ACs and Model-AC are error prone in nonrigid regions and anatomical variations.[15] It appears that the AC provided by the HSEG is suitable for challenging regions such as the pelvic and prostate region, common targets of PET/MRI imaging.

It seems that using the deep learning methods[37,39,40] (such as neural network algorithms) accompanied with the HSEG help to decrease the bias in PET-MRAC5c because of assigning the attenuation coefficients in μ-map as patient specific. Although HSEG is direct and patient-based like SEG and UTE-based segmentation methods, its performance in bony tissue with implants or pathological variations such as sclerotic/lytic bony lesions and certain conditions (eg, myelofibrosis, mastocytosis, osteopetrosis) should be evaluated. The lack of clinical evaluation is the main limitation of the present study.

Conclusion

This study proposes and evaluates a novel hybrid strategy (dedicated Dual TE imaging and multistep segmentation) for generation of a pelvis $\mu\text{-map}_{MR5c}$ for use in MRAC for PET/MRI systems. Positron emission tomography-MRAC reveals that the proposed strategy can decrease uptake bias in the prostate region, a challenging region in clinical PET/MRI systems. Separation of cortical bone, internal and external air, soft tissue, and fat regions using the proposed strategy is the novelty of this work. The suggested approach can improve the accuracy of tracer uptake estimation in a large FOV, in particular for the prostate, on clinical PET/MRI imaging.

Declaration of Conflicting Interests

The author(s) declared no potential conflicts of interest with respect to the research, authorship, and/or publication of this article.

Funding

The author(s) disclosed receipt of the following financial support for the research, authorship, and/or publication of this article: This work was supported under grant #25095 from Tehran University of Medical Sciences, Tehran, Iran.

Reference

1. Zaidi H, Del Guerra A. An outlook on future design of hybrid PET/MRI systems. *Med Phys*. 2011;38(10):5667–5689.
2. Souvatzoglou M, Eiber M, Martinez-Moeller A, et al. PET/MR in prostate cancer: technical aspects and potential diagnostic value. *Eur J Nucl Med Mol Imaging*. 2013;40(suppl 1):79–88.
3. Shandiz MS, Toosi MB, Farsi S, Yaghobi K. Local reference dose evaluation in conventional radiography examinations in Iran. *J Appl Clin Med Phys*. 2014;15(2):4550.
4. Boss A, Weiger M, Wiesinger F. Future image acquisition trends for PET/MRI. *Semin Nucl Med*. 2015;45(3):201–211.
5. Martinez-Möller A, Souvatzoglou M, Delso G, et al. Tissue classification as a potential approach for attenuation correction in whole-body PET/MRI: evaluation with PET/CT data. *J Nucl Med*. 2009;50(4):520–526.
6. Schulz V, Torres-Espallardo I, Renisch S, et al. Automatic, three-segment, MR-based attenuation correction for whole-body PET/MR data. *Eur J Nucl Med Mol Imaging*. 2011;38(1):138–152.
7. Sekine T, ter Voert EE, Warnock G, et al. Clinical evaluation of zero-echo-time attenuation correction for brain 18F-FDG PET/MRI: comparison with atlas attenuation correction. *J Nucl Med*. 2016;57(12):1927–1932.
8. Hofmann M, Steinke F, Scheel V, et al. MRI-based attenuation correction for PET/MRI: a novel approach combining pattern recognition and atlas registration. *J Nucl Med*. 2008;49(11):1875–1883.
9. Paulus DH, Quick HH, Geppert C, et al. Whole-body PET/MR imaging: quantitative evaluation of a novel model-based MR attenuation correction method including bone. *J Nucl Med*. 2015;56(7):1061–1066.
10. Defrise M, Rezaei A, Nuyts J. Time-of-flight PET data determine the attenuation sinogram up to a constant. *Phys Med Biol*. 2012;57(4):885.
11. Khateri P, Rad HS, Jafari AH, et al. Generation of a four-class attenuation map for MRI-based attenuation correction of pet data in the head area using a novel combination of STE/Dixon-MRI and FCM Clustering. *Mol Imaging Biol*. 2015;17(6):884–892.
12. Berker Y, Franke J, Salomon A, et al. MRI-based attenuation correction for hybrid PET/MRI systems: a 4-class tissue segmentation technique using a combined ultrashort-echo-time/Dixon MRI sequence. *J Nucl Med*. 2012;53(5):796–804.
13. Boellaard R, Quick HH. Current image acquisition options in PET/MR. *Semin Nucl Med*. 2015;45(3):192–200.

14. Sekine T, Buck A, Delso G, et al. Evaluation of atlas-based attenuation correction for integrated PET/MR in human brain: application of a head atlas and comparison to true CT-based attenuation correction. *J Nucl Med*. 2016;57(2):215–220.
15. Hofmann M, Bezrukov I, Mantlik F, et al. MRI-based attenuation correction for whole-body PET/MRI: quantitative evaluation of segmentation- and atlas-based methods. *J Nucl Med*. 2011;52(9): 1392–1399.
16. Keereman V, Van Holen R, Mollet P, Vandenberghe S. The effect of errors in segmented attenuation maps on PET quantification. *Med Phys*. 2011;38(11):6010–6019.
17. Samarin A, Burger C, Wollenweber SD, et al. PET/MR imaging of bone lesions–implications for PET quantification from imperfect attenuation correction. *Eur J Nucl Med Mol Imaging*. 2012; 39(7):1154–1160.
18. Akbarzadeh A, Ay MR, Ahmadian A, Alam NR, Zaidi H. MRI-guided attenuation correction in whole-body PET/MR: assessment of the effect of bone attenuation. *Ann Nucl Med*. 2013; 27(2):152–162.
19. Martinez-Möller A, Nekolla SG. Attenuation correction for PET/MR: problems, novel approaches and practical solutions. *Z Med Phys*. 2012;22(4):299–310.
20. Arabi H, Zaidi H. Magnetic resonance imaging-guided attenuation correction in whole-body PET/MRI using a sorted atlas approach. *Med Image Anal*. 2016;31:1–15.
21. Keereman V, Mollet P, Berker Y, Schulz V, Vandenberghe S. Challenges and current methods for attenuation correction in PET/MR. *Magn Reson Mater Mhy*. 2013;26(1):81–98.
22. Catana C, van der Kouwe A, Benner T, et al. Toward implementing an MRI-based PET attenuation-correction method for neurologic studies on the MR-PET brain prototype. *J Nucl Med*. 2010; 51(9):1431–1438.
23. An HJ, Seo S, Kang H, et al. MRI-based attenuation correction for PET/MRI using multiphase level-set method. *J Nucl Med*. 2016; 57(4):587–593.
24. Akbari A, Abbasi-Rad S, Rad HS. T1 correlates age: A short-TE MR relaxometry study in vivo on human cortical bone free water at 1.5 T. *Bone*. 2016;83:17–22.
25. Khateri P, Rad HS, Fathi A, Ay MR. Generation of attenuation map for MR-based attenuation correction of PET data in the head area employing 3D short echo time MR imaging. *Nucl Instrum Meth A*. 2013;702:133–136.
26. Shandiz MS, Rad HS, Ghafarian P, Karam MB, Akbarzadeh A, Ay MR. MR-guided attenuation map for prostate PET-MRI: an intensity and morphologic-based segmentation approach for generating a five-class attenuation map in pelvic region. *Ann Nucl Med*. 2017;31(1):29–39.
27. Lim R, Shapiro M, Wang E, et al. 3D time-resolved MR angiography (MRA) of the carotid arteries with time-resolved imaging with stochastic trajectories: comparison with 3D contrast-enhanced Bolus-Chase MRA and 3D time-of-flight MRA. *Am J Neuroradiol*. 2008;29(10):1847–1854.
28. Chuang KS, Tzeng HL, Chen S, Wu J, Chen TJ. Fuzzy c-means clustering with spatial information for image segmentation. *Comput Med Imaging Graph*. 2006;30(1):9–15.
29. Klein S, Staring M, Murphy K, Viergever M, Pluim JP. Elastix: a toolbox for intensity-based medical image registration. *IEEE Trans Med Imaging*. 2010;29(1):196–205.
30. Wang Y, Chiu E, Rosenberg J, Gambhir SS. Standardized uptake value atlas: characterization of physiological 2-deoxy-2-[18F] fluoro-D-glucose uptake in normal tissues. *Mol Imaging Biol*. 2007;9(2):83–90.
31. Thielemans K, Tsoumpas C, Mustafovic S, et al. STIR: software for tomographic image reconstruction release 2. *Phys Med Biol*. 2012;57(4):867.
32. Cabello J, Lukas M, Förster S, Pyka T, Nekolla SG, Ziegler SI. MR-based attenuation correction using ultrashort-echo-time pulse sequences in dementia patients. *J Nucl Med*. 2015;56(3):423–429.
33. Juttukonda MR, Mersereau BG, Chen Y, et al. MR-based attenuation correction for PET/MRI neurological studies with continuous-valued attenuation coefficients for bone through a conversion from R2* to CT-Hounsfield units. *Neuroimage*. 2015;112:160–168.
34. Delso G, Carl M, Wiesinger F, et al. Anatomic evaluation of 3-dimensional ultrashort-echo-time bone maps for PET/MR attenuation correction. *J Nucl Med*. 2014;55(5):780–785.
35. Shandiz MS, Arabi MH, Ghafarian P, Karam MB, Rad HS, Ay MR. A hybrid method for generation of attenuation map for MR-based attenuation correction of PET data in prostate PET/MR imaging. *EJNMMI Phys*. 2014;1(suppl 1):A77.
36. Leynes AP, Yang J, Shanbhag DD, et al. Hybrid ZTE/Dixon MR-based attenuation correction for quantitative uptake estimation of pelvic lesions in PET/MRI. *Med Phys*. 2017;44(3):902–913.
37. Liu F, Jang H, Kijowski R, Bradshaw T, McMillan AB. Deep learning MR imaging-based attenuation correction for PET/MR imaging. *Radiology*. 2017;286(2):676–684.
38. Marshall HR, Patrick J, Laidley D, et al. Description and assessment of a registration-based approach to include bones for attenuation correction of whole-body PET/MRI. *Med Phys*. 2013;40(8):082509.
39. Leynes AP, Yang J, Wiesinger F, et al. Direct pseudoCT generation for pelvis PET/MRI attenuation correction using deep convolutional neural networks with multi-parametric MRI: zero echo-time and dixon deep pseudoCT (ZeDD-CT). *J Nucl Med*. 2017;59(5):852–858.
40. Hwang D, Kim KY, Kang SK, et al. Improving accuracy of simultaneously reconstructed activity and attenuation maps using deep learning [published online February 15, 2018]. *J Nucl Med*. 2018. doi: 10.2967/jnumed.117.202317.